J. Fluid Mech. (1999), *vol.* 387, *pp.* 321–341. Printed in the United Kingdom

Control of long-wavelength Marangoni–Bénard convection

By A. C. OR, R. E. KELLY, L. CORTELEZZI AND J. L. SPEYER

Department of Mechanical, Aerospace and Nuclear Engineering, University of California, Los Angeles, CA 90095-1597, USA

(Received 1 May 1998 and in revised form 25 September 1998)

A nonlinear feedback control strategy for delaying the onset and eliminating the subcritical nature of long-wavelength Marangoni–Bénard convection is investigated based on an evolution equation. A control temperature is applied to the lower wall in a gas–liquid layer otherwise heated uniformly from below. It is shown that, if the interface deflection is assumed to be known via sensing as a function of both horizontal coordinates and time, a control temperature with a cubic-order polynomial dependence on the deflection is capable of delaying the onset as well as eliminating the subcritical instability altogether, at least on the basis of a weakly nonlinear analysis. The analytical results are supported by direct numerical simulations. The control coefficients required for stabilization are $O(1)$ for both delaying onset indefinitely and eliminating subcritical instability. In order to discuss the effects of control, a review is made of the dependence of the weakly nonlinear subcritical solutions without control upon the various governing parameters.

1. Introduction

The long-wavelength mode of Marangoni–Bénard convection (Scriven & Sternling 1964; Smith 1966) is the most dangerous mode of instability if the layer of fluid is sufficiently thin, or when it is subjected to reduced gravity. A number of studies of the instability have been made by means of an evolution equation derived in the long-wavelength limit. A review of this equation and its development is given by Oron, Davis & Bankoff (1997). These studies reveal that the properties of this instability are substantially different from convection of the finite-wavelength cellular type (Pearson 1958). Funada & Kotani (1986) and Funada (1987) showed that steady finite-amplitude solutions exist in a region below the neutral curve predicted by linear theory. Due to the subcritical nature of the instability, the region below the neutral curve is only conditionally stable. Initial disturbances with sufficiently small amplitude will decay to the no-motion state but those with large enough amplitude will diverge. Besides spatially periodic finite-amplitude solutions, localized solutions of the solitary type are also possible.

Recently, an extension of the one-layer model to a gas–liquid model was performed by VanHook *et al.* (1997), who demonstrated that a two-fluid model is essential for producing good agreement with experimental observations obtained from a two-fluid layer bounded above and below by rigid walls. The authors performed both a weakly nonlinear analysis and direct numerical simulations based on a more general evolution equation than that used by Funada, in which the nonlinearity is not necessarily

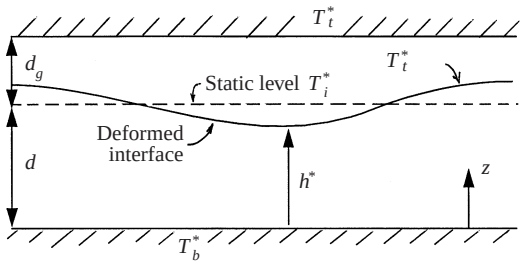

FIGURE 1. Geometric configuration.

assumed to be small. Their results are consistent with those reported by Funada (1987) in that steady solutions can only be found below the linear neutral curve. But unlike Funada's one-layer result which only gives surface deformations of depression, both elevated and depressed type interfacial deformations are possible in the gas–liquid model, depending on the Biot numbers involved. Based on numerical simulations of the two-fluid model and experimental observations, VanHook *et al.* (1997) reported that no forward branch of solution connected to the unstable subcritical branch of solution has been found. On the other hand, the parameter regime explored by the authors in the fully numerical simulations is limited. It will be pointed out later that for a certain range of the parameter associated with a depressed interface the cubic nonlinear term is stabilizing and therefore a stable forward branch is possible.

From the viewpoint of applications, the long-wavelength mode of instability can be detrimental for many processes involving heat transfer or material processing due to its tendency to rupture the surface. A natural question arising is whether this mode of instability can be suppressed or modified in such a way that the subcritical region can be stable even for finite-amplitude disturbances. The current analysis, though restricted to a regime near the critical point based on an amplitude expansion up to the cubic term, indicates that the answer is affirmative.

Our control strategy basically applies a principle similar to that used by Tang & Bau (1994) for controlling Rayleigh–Bénard convection, which is as follows. Assume that a certain variable describing the instability can be measured so that complete knowledge of this variable is available in both space and time. We can feed this information back into the dynamics in terms of a function of another variable that can affect the instability, such as, in the case of Tang & Bau (1994), a control temperature. In fact, Bau (1999) has shown independently how such a control can delay the onset of thermocapillary convection on a linear basis, although a different sensing mechanism is used than the one we employ. But unlike these authors who demonstrated control of a single but arbitrary Fourier component of the instability, we use the control temperature to affect directly an actual localized disturbance arising from the long-wavelength instability. Our approach is equivalent to assuming control over a continuous bandwidth of wavenumbers in Fourier space in the problem of Tang & Bau (1994). As for the use of a nonlinear control law in the present study, our strategy appears to be more akin to another study done on the control of the planform of Rayleigh–Bénard convection by Shortis & Hall (1996). However, Yuen & Bau (1996) have shown how a cubic-order nonlinear control can prevent the onset of a subcritical bifurcation of a secondary instability in the problem of one-dimensional flow in a convection loop, which is governed by the Lorenz equations.

For our problem, the control law governs an actuating temperature, $T_c(x, y, t)$,

applied on the lower wall as a polynomial function of the interfacial deflection, η,

$$T_c = K_1\eta + K_2\eta^2 + K_3\eta^3 + \cdots, \tag{1}$$

where $\eta = h - 1$, so that, with reference to figure 1, the deflection is measured from the mean position of the interface. Thus, the actuating temperature T_c is zero for the undisturbed basic state, which is different from the model used by Shortis & Hall (1996) but similar to that of Tang & Bau (1994). The constants K_i ($i = 1, 2, 3, \ldots$), or gains, will be determined later by means of analysis. In the present study, the first three leading terms in the polynomial will be used. The linear term in (1) is responsible for changing the value of the critical Marangoni number. Depending on how much forward shift of the bifurcation point is desirable, K_1 can be determined. The linear term will modify the next-order nonlinear terms via change of the structure of the linear solutions. The second term in (1), K_2, can then be chosen to remove the quadratic-order nonlinearity from the evolution equation, which is essential for the removal of subcritical instability. Both the first- and second-order control terms will affect the cubic-order nonlinearity. After the quadratic-order term is eliminated, the cubic-order nonlinearity controls the dynamics. Subcriticality or supercriticality of the bifurcation then depends only on the sign of the cubic-order term. If we pick the right sign for K_3, it is possible to create a supercritical bifurcation. Besides allowing convection to occur at a higher value of Marangoni number, a supercritical bifurcation might be preferred because it is less sensitive to environmental noise.

We review the derivation of the evolution equation with control incorporated in § 2. In § 3, the weakly nonlinear solutions with no control are reviewed and further investigated. The control strategy and analysis as well as the supercritical solutions in the controlled case are studied in § 4. In § 5, we provide more results based on direct numerical simulation. Finally, some concluding remarks will be given in § 6.

2. Mathematical formulation

Numerous authors have studied the one-layer version of the evolution equation which has since been extended into a gas–liquid version by VanHook *et al.* (1997; see their paper or Oron *et al.* (1997) for the earlier references). The gas–liquid model takes into account the ratios of thermal properties and thicknesses of the fluids but assumes that the upper fluid density is much smaller than that of the lower fluid so that the motion of fluid above the interface can be neglected. Consider the fluid model shown in figure 1. The static depths of the liquid and gas are, respectively, d and d_g; the thermal diffusivities are κ and κ_g. The bottom, top and static interfacial temperatures are, respectively, T_b^*, T_t^* and T_i^*. In the situation with control, an additional temperature T_c^* is imposed on the bottom wall. Length, time, velocity, pressure and temperature are scaled by quantities d, d^2/κ, κ/d, $\rho\nu\kappa/d^2$ and $\Delta T^* = T_b^* - T_i^*$, respectively.

An evolution equation can be obtained from the Navier–Stokes and energy equations by assuming that the horizontal characteristic scale of the unstable modes, L, is much greater than either d or d_g. In other words, the fundamental wavenumber, defined by $q = 2\pi d/L$, is a small parameter with which the basic equations can be expanded. The expansion procedure gives rise to an evolution equation governing the local interfacial depth h. But before we proceed, it is important to understand the scaling scheme appropriate to the long-wavelength expansion. In this scheme, the interfacial height, the vertical coordinates, the vertical and horizontal velocities, and the temperature and pressure are scaled, respectively, according to: $h \sim O(1)$, $\partial_z \sim O(1)$,

$w \sim O(q^2)$ and $\boldsymbol{u}_\perp \sim O(q)$, $T \sim O(1)$ and $P \sim O(1)$. In deriving the evolution equation, the variables of the basic equations are accurate up to the leading orders given above. The equation of state for surface tension, σ, is given by $\sigma = \sigma_0 + \gamma_0(T^* - T_b^*)$, in which the first term on the right is assumed to be significantly larger than the amplitude of the second term. The normal-stress condition can be considered temperature independent and dependent on σ_0 only. The tangential-stress condition, on the other hand, depends on γ_0 but not on σ_0. In a non-dimensional form the equation of state is then

$$S = S_0 + M(T - T_b), \tag{2}$$

where S_0 is the reference surface tension defined by $S_0 = \sigma_0 d/\rho\nu\kappa$ and M is the Marangoni number defined by $M = \gamma_0 d\Delta T^*/\rho\nu\kappa$. Here, γ_0 denotes the derivative of surface tension with respect to temperature at the reference value.

The long-wavelength evolution equation has the following form:

$$\partial_\tau h + \nabla \cdot \left\{ -\tfrac{3}{2} D \left(\frac{\mathrm{d}T}{\mathrm{d}h} \right) h^2 \nabla h - h^3 \nabla h + \frac{q^2}{B} h^3 \nabla \nabla^2 h \right\} = 0 \,, \tag{3}$$

which is identical to equation (3.12) of VanHook *et al.* (1997) for the uncontrolled case. In the above equation, $h(X, Y, \tau)$ is the non-dimensional local thickness of the liquid where $X = qx$ and $Y = qy$ are stretched horizontal coordinates and $\tau = \frac{1}{3} G q^2 t$ is defined as a slow time with G being the Galileo number defined by $G = gd^3/\nu\kappa$. The operator ∇ denotes the horizontal Laplacian in stretched coordinates. The two major parameters D and B are defined by $D = M/G$ and $B = G/S_0$ (notice our B/q^2 corresponds to the definition of B in VanHook *et al.* 1997; we later denote B/q^2 as B_v). The parameter B is the usual Bond number whereas VanHook *et al.* (1997) refer to D^{-1} as the 'dynamic Bond number', where σ_0 is replaced by $\gamma_0 \Delta T^*$. The three terms inside the wavy brackets on the right-hand side of (3) represent, respectively, thermocapillary, gravity and surface-tension effects.

In the evolution equation, the surface-tension term corresponds to a fourth-order derivative in the horizontal coordinates. Many authors (e.g. Deissler & Oron 1992; VanHook *et al.* 1997) retain this term even for $q \ll 1$ by introducing the scaling relationship $B \sim O(q^2)$, which is often referred to as the strong surface-tension limit (see Simanovskii & Nepomnyashchy 1993), although it is also appropriate for the microgravity case with $S_0 \sim O(1)$. In the long-wavelength expansion, $q \to 0$ is assumed but B then becomes artificially small as $q \to 0$. But without a strong-surface-tension scaling relationship, the surface-tension term in general is two orders of magnitude in q smaller than the other terms, unless a re-scaling of the equation is introduced for near critical conditions. This re-scaling will give a lower-order nonlinear equation (see Funada 1987; Simanovskii & Nepomnyashchy 1993). In both controlled and uncontrolled convection, we shall first consider the re-scaled version of the equation with fixed S_0 in order to obtain the behaviour of instability close to the bifurcation point. After we have gained a better understanding of the behaviour at low-order, then we shall invoke the strong-surface-tension, weakly nonlinear version of the equation by retaining up to the cubic-order nonlinear term in order to obtain the qualitative behaviour of the bifurcated solutions further away from the critical point. Note that the large surface tension case corresponds to small B, and so it also corresponds to microgravity conditions.

The interfacial temperature $T(h)$ can be computed in the small-q limit so that the heat transfer is locally conductive (and quasi-steady) between the upper and lower walls. According to our scaling, the basic temperatures at $z = 0$, 1 and $(1 + d_g/d)$

are 0, -1 and $-(1+H^{-1})$, respectively, where H is known as the one-layer Biot number defined by $H = k_g d/k d_g$. When control is applied, the lower-wall temperature becomes T_c. In the long-wavelength limit, the interfacial temperature at the deformed interface, $T(h)$, can be computed from the condition of continuity of heat flux at the interfacial surface. Since the temperature gradient in each layer is constant, this condition can be written as

$$\frac{T_c - T(h)}{h} = \left(\frac{k_g}{k}\right) \frac{T(h) + 1 + H^{-1}}{1 - h + d_g/d}\ , \tag{4}$$

where the two-layer Biot number $F = (d/d_g - H)/(1+H)$ is defined (see VanHook *et al.* 1997). Note that $F \geqslant 0$ if $k \geqslant k_g$. If we substitute the two ratios in the above equation, d_g/d and k_g/k, by H and F and with some algebraic manipulations, we obtain the following expression for $T(h)$:

$$T(h) = T_0(h) + T_c \left(1 + \frac{H}{1+H} T_0(h)\right), \tag{5}$$

where $T_0(h)$ denotes the non-dimensional temperature in the absence of control (see also equation (3.6*j*) of VanHook *et al.* 1997), namely,

$$T_0(h) = -\frac{h}{1 - F(h-1)}\ . \tag{6}$$

The first two terms within the wavy bracket of (3) are $O(1)$, while the third term is of $O(q^2)$ for fixed B. When D is at the critical value D_c for which $q \to 0$, the sum of the first two terms vanishes. For D slightly different from D_c, there is an $O(q^2)$ proximity in which a balance between the sum of these two terms and the $O(q^2)$ surface-tension term exists if $h - 1 \sim O(q)$ is assumed.

We now substitute (1) for T_c into (5) and $1+\eta$ for h. Then (3) gives

$$\partial_\tau \eta + \nabla \cdot \Big\{ (1+\epsilon)\Psi - \hat{K}_1 \Theta_1 - \hat{K}_2 \Theta_2 - \hat{K}_3 \Theta_3 - (1+\eta)^3 + \frac{(1+\eta)^3 q^2}{B} \nabla^2 \Big\} \nabla \eta = 0, \tag{7}$$

where the $\hat{K}_i$ are a set of normalized parameters defined by

$$\hat{K}_i = \frac{3DK_i}{2(1+H)} \quad \text{for} \quad i = 1, 2, 3, \tag{8}$$

and

$$\epsilon = \tfrac{3}{2} D(1+F) - 1 \tag{9}$$

measures the degree of supercriticality for the linear, uncontrolled case. In terms of η, we obtain

$$\Psi(\eta) = 1 + 2(1+F)\eta + (1+F)(1+3F)\eta^2 + \cdots, \tag{10}$$

$$\Theta_1(\eta) = 1 + 2(1 - H(1+F))\eta + (1 - H(1+F)(3F+4))\eta^2 + \cdots, \tag{11}$$

$$\Theta_2(\eta) = 2\eta + (4 - 3H(1+F))\eta^2 + \cdots, \tag{12}$$

and

$$\Theta_3(\eta) = 3\eta^2 + \cdots. \tag{13}$$

After summing up the terms appearing in the wavy brackets of (7) other than the

term involving B^{-1}, we obtain

$$\begin{aligned}\Lambda &\equiv (1+\epsilon)\Psi - \hat{K}_1\Theta_1 - \hat{K}_2\Theta_2 - \hat{K}_3\Theta_3 - (1+\eta)^3 \\ &= (\epsilon - \hat{K}_1) + (2F - 1 - a_1\hat{K}_1 - 2\hat{K}_2)\eta \\ &\quad + (3F^2 + 4F - 2 - a_2\hat{K}_1 - b_2\hat{K}_2 - 3\hat{K}_3)\eta^2 + \cdots, \end{aligned} \tag{14}$$

where $a_1 = 2(1-H(1+F))$, $a_2 = 1-H(1+F)(3F+4)$ and $b_2 = 4-3H(1+F)$. These coefficients may vanish for certain parameter values of H and F. In the examples given, however, we assume that they are non-zero. Now, (7) can be rewritten as

$$\partial_\tau \eta + \nabla \cdot \left\{ \Lambda + \frac{(1+\eta)^3 q^2}{B} \nabla^2 \right\} \nabla \eta = 0\,. \tag{15}$$

For the purpose of later analysis, the above equation for the uncontrolled and controlled situations will be treated separately and the equation will be re-scaled in the region near the critical point.

Re-scaled equations for uncontrolled convection

First, we consider the uncontrolled situation. In this case, the $\hat{K}_i$ $(i = 1, 2, 3)$ vanish. Equation (14) becomes

$$\Lambda = \epsilon + (2F-1)\eta + (3F^2 + 4F - 2)\eta^2 + \cdots. \tag{16}$$

Because the strong-surface-tension assumption is not used, a factor of q^2/B appears with the surface tension term in (7). A lowest-order balance can be achieved by rescaling ϵ, η and t as follows:

$$\epsilon = q^2 R, \quad \eta = q^2 A, \quad T = q^2 \tau, \tag{17}$$

where R, A and T (note: the second slow time T uses the same notation as temperature) are $O(1)$ quantities. Thus, we are in an $O(q^2)$ neighbourhood of criticality where the growth rates are $O(q^4)$ using unscaled non-dimensional variables. The quadratic term in (16) is $O(q^2)$ relative to the other terms. This balance yields the following evolution equation, to $O(q^2)$:

$$\partial_T A + \nabla \cdot \left\{ R + \frac{1}{B}\nabla^2 + (2F-1)A \right\} \nabla A \;=\; 0. \tag{18}$$

In this balance, only the quadratic-order nonlinearity is retained. In the special case when $F = 0.5$, the quadratic nonlinear term vanishes so that we must take into account the next-order cubic nonlinear term. This case will be discussed later in § 3.1.

Re-scaled equation for controlled convection

The term $(\epsilon - \hat{K}_1)$ in (14) represents the shift in the critical value of M due to linear control (see § 4). Our control strategy is to eliminate the subcritical steady solutions, at least on a weakly nonlinear basis. The way to accomplish this goal is to diminish the quadratic term so that the cubic nonlinear term becomes the dominant term. To do this, we go back to (14). For the $O(\eta)$ term to be of the same order as the $O(\eta^2)$ term, we require the coefficient of the $O(\eta)$ term to be of $O(q)$. Thus, we impose the following condition:

$$F - \tfrac{1}{2} - \tfrac{1}{2}a_1\hat{K}_1 - \hat{K}_2 = \alpha q, \tag{19}$$

where α is a parameter of $O(1)$ which models any residual quadratic effect due, say, to detuning. The $O(1)$ balance in (19) determines the value of $\hat{K}_2$ in terms of $\hat{K}_1$,

that is,

$$\hat{K}_2 = F - \tfrac{1}{2} - \tfrac{1}{2}a_1\hat{K}_1. \tag{20}$$

This condition enables us to eliminate $\hat{K}_2$ in favour of $\hat{K}_1$ and $\hat{K}_3$ so that the final scheme involves a two-gain representation. The new scalings corresponding to (17) to be introduced for the control situation are: $\epsilon - \hat{K}_1 = q^2R$, $\eta = qA$ and $T = q^2\tau$. The following evolution equation is then obtained:

$$\partial_T A + \nabla \cdot \left\{ R + \frac{1}{B}\nabla^2 + \alpha A + \beta A^2 \right\} \nabla A \;=\; 0, \tag{21}$$

where R, α and β are again $O(1)$ parameters and A is of $O(1)$. Note that a different scaling on η than that in the uncontrolled case is used, due to the reduction in magnitude of the quadratic term. As a result, the cubic term appears in (21) whereas it is of higher order in (18).

In (21), both R and α are independent of the gains. Their values can be imposed arbitrarily. On the other hand, the parameter β depends on the control gains in the following manner:

$$\beta = \beta_0 + \beta_1\hat{K}_1 - 3\hat{K}_3, \tag{22a}$$

where

$$\beta_0 = 3(1+H)F^2 + \tfrac{3}{2}HF - \tfrac{3}{2}H, \tag{22b}$$

$$\beta_1 = 3(1+H)HF^2 + 6H^2F + 3(H^2 - H + 1). \tag{22c}$$

The parameter β controls the sign of the cubic nonlinear coefficient, which determines the subcriticality and supercriticality of the bifurcation at this order. If the quadratic term had not been eliminated, subcritical convection would still occur but control of the finite-amplitude convection could be exerted via $\hat{K}_3$. However, the scaling of the controlled case would then hold, and so large values of $\hat{K}_3 \sim O(q^{-2})$ would be required for such control. For $R > 0$, it is clear that we need $\beta < 0$ to achieve a steady finite-amplitude state, and so $\hat{K}_3 > 0$ is desirable for this purpose. In § 4 more analysis of the above control strategy, including examples and a summary of results, will be given.

3. Solutions for uncontrolled convection

Besides Funada & Kotani (1986) and Funada (1987) who analysed the weakly nonlinear evolution equations, Simanovskii & Nepomnyashchy (1993, § 3.3) present a brief description of the equations with quadratic and cubic nonlinearity and their solutions (see their equations (3.46) and (3.57) for more details). For this reason, an extensive analysis will not be done here. But it is worthwhile to illustrate the bifurcation characteristics and explore the weakly nonlinear regime since experimental results are now available (VanHook *et al.* 1997). It is also desirable to have a better idea of how the weakly nonlinear solutions depend upon the parameters involved in order to discuss the effect of control.

We observe that previous studies, notably Deissler & Oron (1992) and VanHook *et al.* (1997), suggest that the flow field is in general associated with axisymmetric surface deformations (see VanHook *et al.* figure 9). In this paper, we shall treat both the one-dimensional rectilinear and the axisymmetric cases. The rectilinear case is simple enough to permit an explicit analysis, which will provide a better understanding of the instability. The axisymmetric case is more relevant to experimental observations.

Subcritical steady solutions

In this subsection we present the nonlinear one-dimensional solutions and bifurcation characteristics for the rectilinear case. Emphasis will be placed on the one-dimensional solutions because we will later examine the effect of feedback control on such disturbances. Here an explicit analysis is given based on (18). We integrate the steady form of (18) once to give

$$\left(R + \frac{1}{B}\partial_{XX}\right)\partial_X A + (2F-1)(A\partial_X A) \ = c_3 \ . \tag{23}$$

A second integration of the above equation gives

$$\left(R + \frac{1}{B}\partial_{XX}\right)A + (2F-1)\tfrac{1}{2}A^2 \ = c_2 + c_3 X. \tag{24}$$

For bounded steady solutions, the constant of integration c_3 is set to zero. Then both sides of the equation are multiplied by $\partial_X A$, and another integration gives

$$\frac{1}{B}(\partial_X A)^2 = c_1 + c_2 A - RA^2 - \frac{(2F-1)}{3}A^3. \tag{25}$$

This equation certainly can be integrated once more to give A in terms of a Jacobi-Elliptic integral. Only the cnoidal modes are presented here. Cnoidal solutions can be expressed in terms of Jacobi-Elliptic functions (e.g. see Abramowitz & Stegun (1972) and *MATLAB* under special functions). Using a short notation, one such function, $\mathrm{cn}(u,m)$, is written here as $\mathrm{cn}u$. The parameter m has values between zero and one. Consider a solution of the form $A(X) = A_0 + A_s\mathrm{cn}^2(\lambda X, m)$ where A_0 is a constant corresponding to a shift of reference level. The differential equation satisfied by $\mathrm{cn}^2(u)$ where $u = \lambda X$ is

$$\left(\frac{\mathrm{dcn}^2 u}{\mathrm{d}u}\right)^2 = 4\mathrm{cn}^2 u(1-\mathrm{cn}^2 u)(1-m^2+m^2\mathrm{cn}^2 u). \tag{26}$$

In terms of $A - A_0$ and X, this equation can be written as

$$(\partial_X(A-A_0))^2 = \lambda^2 A_s^2\left(\frac{4(1-m^2)}{A_s}(A-A_0) + \frac{(2m^2-1)}{A_s^2}(A-A_0)^2 - \frac{4m^2}{A_s^3}(A-A_0)^3\ \right). \tag{27}$$

By comparison with (25), the coefficient of the linear $(A-A_0)$ term on the right-hand side gives the constant c_2. The quadratic and cubic terms in $(A-A_0)$ give the following relationships for the phase and amplitude:

$$\lambda^2 = \frac{RB}{4(1-2m^2)}\ , \quad A_s = \frac{12\lambda^2 m^2}{B(2F-1)}\ . \tag{28}$$

By expanding the terms involving $(A-A_0)$, the constant term independent of A gives c_1 in terms of A_0. We note that for $0 \leqslant m < 1/\sqrt{2}$ the cnoidal modes correspond to $R > 0$ but below the linear neutral curve. For $1/\sqrt{2} < m \leqslant 1$ the cnoidal modes are strictly subcritical (i.e. $R < 0$). Since both the critical R and λ occur at zero, it is important to note that $\lambda \sim R^{1/2}$.

There are two limits of interest. The first one corresponds to $m \to 0$, for which $\mathrm{cn}(u,m) \to \cos(u)$. But as $m \to 0$, we also have $A \to 0$ so that the nonlinear term becomes negligible. In this case, we obtain $R = 4\lambda^2/B$ and the solution becomes

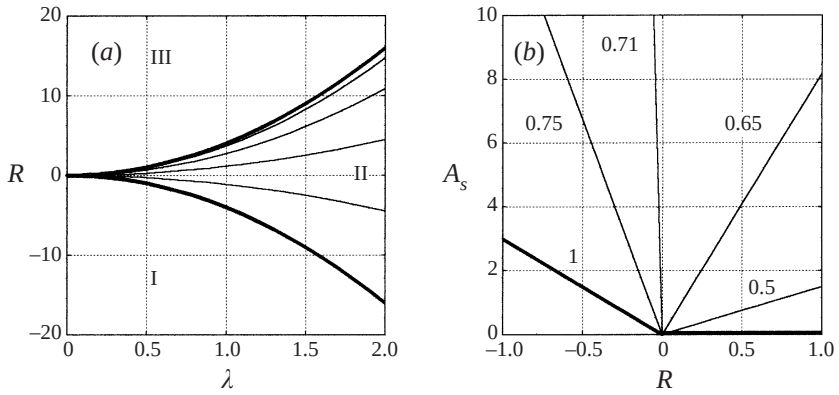

FIGURE 2. Stability diagrams showing the linear neutral curve and nonlinear equilibrium curves for (*a*) R versus λ and (*b*) A_s versus R.

$(A - A_0) = A_s \cos^2 \lambda X$ where A_s becomes arbitrary. We rewrite the equation as $A = A_0 + A_s(1 + \cos(2\lambda X))/2$ and choose $A_0 = -A_s/2$ so that the solution becomes $A = (A_s/2)\cos(2\lambda X)$. This choice of A_0 can be extended to the fully nonlinear solution by imposing the mean level of A as the reference level. If we denote $k = 2\lambda$, then from the phase equation (28) the neutral curve $R = k^2/B$ is recovered (for $m \to 0$). The cnoidal solution limit with $m \to 0$ therefore corresponds to the linearized problem. The amplitude of solutions is linear in R, just as for a bifurcation of a transcritical type.

The second limit corresponds to $m \to 1$, for which cn$u \to$ sech$u$ as $m \to 1$. Therefore we obtain $A = A_0 + A_s \operatorname{sech}^2 \lambda X$ where

$$R = -\frac{4\lambda^2}{B}, \quad A_s = \frac{12\lambda^2}{B(2F - 1)} \tag{29}$$

and A_0 is determined by $\int_{-\infty}^{\infty} A \mathrm{d}X = 0$. A solitary solution can exist only for $R < 0$ since λ has to be real. Hence, as R is increased from a large negative value, solitary disturbances can appear first. The amplitude is given by $A_s = -3R/(2F - 1)$. For a given R, this solution gives a localized elevation or depression depending on whether F is greater or smaller than 0.5. This result is consistent with the findings of VanHook *et al.* (1997).

We now illustrate the solution domains. We let $B = 1$ and $F = 1$, since (18) can be normalized to a single parameter corresponding to R. In fact this choice corresponds to the normalized equation. In figure 2(*a*), the upper and lower heavy solid curves correspond, respectively, to the neutral curve and the solitary-solution curve according to (28). These two curves separate the (λ, R)-plane into three distinct regions. In region III both linear and quadratic nonlinear effects are destabilizing and so no steady solution exists. In region II the linear effect is stabilizing but the nonlinear effect is destabilizing. A dynamical balance among thermocapillarity, gravity and surface tension forces exists in this region and gives rise to the family of cnoidal solutions. The four thin lines from the top correspond to $m = 0.2$ to 0.8 in increments of 0.2. In region I the linear effect is dominant. With a sufficiently large spatial scale for the disturbances, disturbances to the basic state will decay in this region. Figure 2(*b*) shows the R versus A_s relationship. The heavy solid line on the right corresponds to the linear solution and the one on the left corresponds to the solitary solution. The number next to each curve denotes the value of m. On the side

of $R < 0$, the solitary-mode shape appears to be the most unstable solution because it gives the lowest bound of A_s. Below the left heavy solid line, the disturbance will decay; above the line, a disturbance will grow. Hence, a critical disturbance amplitude exists that gives rise to the solitary solution. On the side of $R > 0$, the linear effect also becomes destabilizing. The sinusoidal modes corresponding to the linear effect would appear to be the fastest growing ones for a hypothetical situation where the initial value of R is positive.

The evolution equation for the special case $F = 0.5$ at which the quadratic nonlinear term vanishes has to be scaled differently than (17). The scales for this case are similar to those for controlled convection in § 2.2, namely, $\epsilon = q^2 R$, $\eta = qA$ and $T = q^2\tau$. With this scaling at $F = 0.5$, the extended equation becomes

$$\partial_T A + \nabla \cdot \left\{ R + \frac{1}{B}\nabla^2 + \frac{3}{4}A^2 \right\} \nabla A \;=\; 0. \tag{30}$$

The cubic term for this case is destabilizing. It will be demonstrated later, however, that for $F < 0.387$, approximately, the cubic term exerts a stabilizing effect. By including this higher-order term a stable branch of steady-state solution can be obtained. The effect of including the cubic term will be discussed by means of numerical solutions later, from which both axisymmetric and rectilinear solutions can be compared. At $F = 0.5$, (30) becomes the governing equation. Because the coefficient of the cubic nonlinear term is positive, the equation admits the modified solitary solution for $R < 0$ given by

$$A(X) = A_s \operatorname{sech} \lambda X, \tag{31}$$

where $\lambda = \pm(-RB)^{1/2}$ and $A_s = \pm(6\lambda^2/B\beta)^{1/2}$. Again the modified solitary solution is subcritical. But unlike the solitary solution, the modified solitary solution can be either an elevation or depression for a given set of parameters. No steady supercritical ($R > 0$) solution exists for $F = 0.5$. Furthermore, all the steady subcritical solutions are unstable – a conclusion of both Funada (1987) and Simanovskii & Nepomnyashchy (1993).

The one-dimensional rectilinear case discussed above permits an explicit treatment from which the structure of the solutions in the proximity of the bifurcation point can be analysed in detail. In the following, we extend the previous scope of analysis by numerical computations of both axisymmetric steady solutions and the one-dimensional rectilinear solutions when the effect of the cubic nonlinear term is also included.

Numerical solutions

The result of § 3.1 reveals a family of subcritical solutions near the critical point. In order to understand whether the subcritical solutions continue onto other branches of solutions further away from the critical point, the next higher-order nonlinear terms have to be included. In the following we consider a weakly nonlinear version of (15) by retaining up to the cubic-order term in η. Also, in order to retain the surface-tension term, we invoke the strong-surface-tension assumption. In the analysis of this subsection, we assume the factor q^2 is absorbed in the parameter B (see VanHook *et al.* 1997), and so we define $B_v = Bq^{-2}$ where $B_v \sim O(1)$. Up to the cubic-order term (15) becomes

$$\partial_\tau \eta + \nabla \cdot \left\{ \left(\epsilon + \frac{1}{B_v}\nabla^2 + (2F-1)\eta + (3F^2 + 4F - 2)\eta^2 \right) \nabla\eta \right\} = 0. \tag{32}$$

To proceed, a note on the mass conservation property of (32) will be helpful. In the numerical solutions, we consider only fluid of finite horizontal extent. This situation includes the case of a fluid confined by lateral walls and the case of a control volume of an infinite layer of fluid bounded by an imaginary control surface. Integrating the equation over the volume and using the divergence theorem gives

$$\partial_\tau Q = \int_S \left\{ \epsilon + \frac{1}{B_v}\nabla^2 + (2F-1)\eta + (3F^2+4F-2)\eta^2 \right\} (\partial_n \eta) \mathrm{d}S, \quad Q \equiv \int_V \eta \mathrm{d}V. \quad (33)$$

Given the fact that there is no mass flux through the bottom wall and the interface, the flux integral on the right-hand side is over the lateral boundary enclosing the volume of fluid. There are two cases for which the flux integral vanishes. These are: (i) $\partial_x \eta$ vanishes identically at the lateral boundary, (ii) the sum of the four terms inside the wavy bracket of the flux integral of (33) vanishes (in this case, η corresponds to an equilibrium solution). In the two types of solutions we shall consider, namely, axisymmetric solutions and one-dimensional rectilinear solutions with periodic boundary conditions, the flux integral vanishes for both cases. When the flux integral vanishes, then Q is constant in time.

For the axisymmetric steady solutions, in polar coordinates we let $\eta = \eta(r)$. For an arbitrary function $f(r)$ we have the following identities:

$$\nabla f = \boldsymbol{i}_r \frac{\mathrm{d}f}{\mathrm{d}r}, \quad \nabla^2 f = \frac{1}{r}\frac{\mathrm{d}}{\mathrm{d}r}\left(r\frac{\mathrm{d}f}{\mathrm{d}r}\right).$$

Substituting the operators into the above equation and integrating the resulting equation once yields

$$\frac{1}{B_v}\left(r\frac{\mathrm{d}^3\eta}{\mathrm{d}r^3} + \frac{\mathrm{d}^2\eta}{\mathrm{d}r^2}\right) + \{\epsilon + (2F-1)\eta + (3F^2+4F-2)\eta^2\}\left(r\frac{\mathrm{d}\eta}{\mathrm{d}r}\right) = 0. \quad (34)$$

The above problem will be solved by using a finite difference approach and the steady-state solutions are obtained by the Newton–Raphson method. There are numerical steady-state solutions of a cnoidal type. For a given subcritical value of ϵ the solitary solution corresponds to the largest horizontal scale (i.e. smallest λ, see (28)). Since the solitary mode (with localized structure) appears to be the type seen in experiments (VanHook *et al.* 1997), our effort here is to investigate the localized solution resembling the solitary mode. In the above equation the integration constant is set to zero so that $\eta(\infty) = 0$. In the numerical solutions, a finite cut-off radius is chosen at a sufficiently large value, r_{co}, so that we set $\eta(r_{co}) = 0$. The other two boundary conditions to be imposed on the numerical solutions are

$$\frac{\mathrm{d}}{\mathrm{d}r}\eta(0) = 0, \quad \frac{\mathrm{d}}{\mathrm{d}r}\eta(r_{co}) = 0. \quad (35)$$

The rectilinear solutions are obtained from the following one-dimensional equation:

$$\left(\epsilon + \frac{1}{B_v}\partial_{XX}\right)\partial_{XX}\eta + \partial_X\{(2F-1)\eta + (3F^2+4F-2)\eta^2)\partial_X\eta\} = 0. \quad (36)$$

The boundary conditions imposed are periodic at two cut-off points $X = \pm X_{co}$,

$$\eta(-X_{co}) = \eta(X_{co}), \quad \partial_X\eta(-X_{co}) = \partial_X\eta(X_{co}). \quad (37)$$

Again our focus will be the solitary mode. The variation of the rectilinear solutions appears to have slightly longer horizontal scale. The coefficient of the cubic term in (34), (36) is negative (and so stabilizing) only if $F < 0.387$. We will restrict the

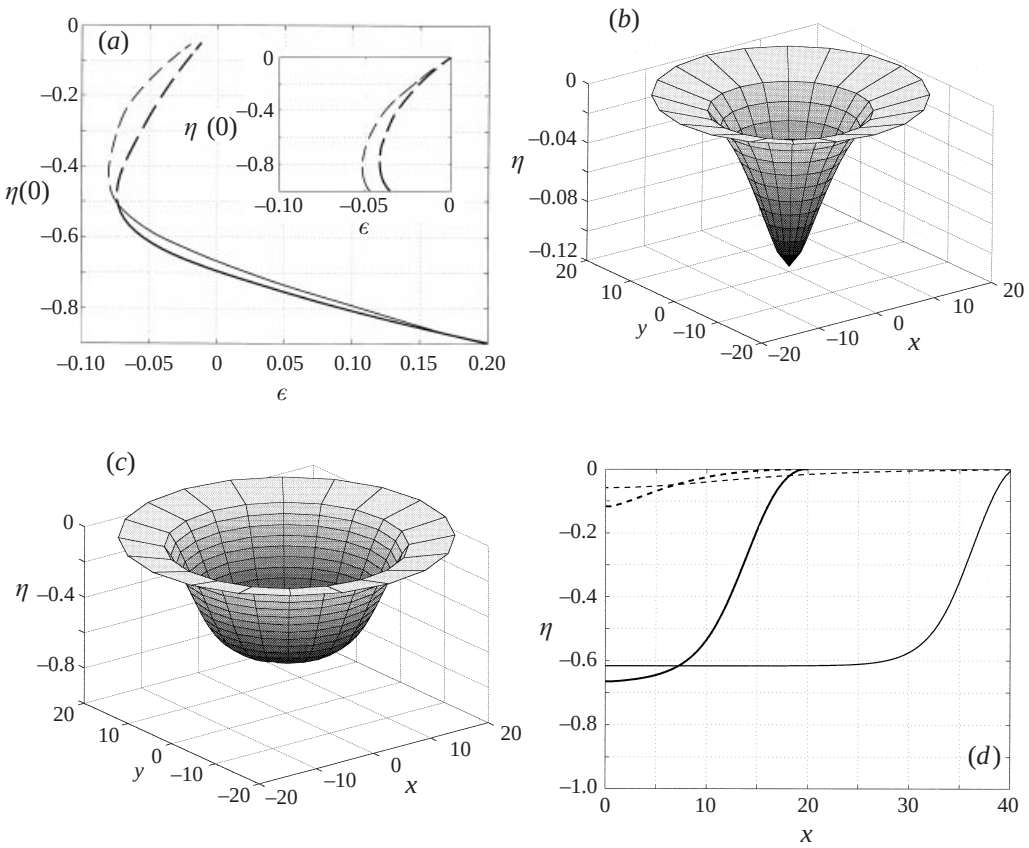

FIGURE 3. (*a*) A comparison between the bifurcation curves for the rectilinear and axisymmetric localized solutions at $B_v = 1$ and $F = 0$ (see the text for details); (*b*) the three-dimensional shape of the axisymmetric localized disturbance (unstable) at $\epsilon = -0.02$ corresponding to the backward branch; (*c*) shape of the axisymmetric localized disturbance (stable) at $\epsilon = -0.02$ corresponding to the forward branch; (*d*) a comparison between the half-sectional shapes of η of the backward-branch solution (dashed) and forward-branch solution (solid) of the axisymmetric mode (heavy lines) and rectilinear mode (thin lines) at $\epsilon = -0.02$.

discussion to this range of F. For larger F, steady forward-branch solutions are not possible at this order.

In figure 3(*a*) we show the bifurcation diagram for both axisymmetric and rectilinear localized solutions corresponding to parameter values $B_v = 1$ and $F = 0$. In the experiment B_v is about an order of magnitude larger whereas F can indeed be close to zero (see VanHook *et al.* 1997, table 2 and § 5). A larger B_v corresponds to a steeper deformation with smaller horizontal scale (see more discussion below). The cut-off length scales are $r_{co} = 20$ and $X_{co} = 40$ for the two types of solutions, respectively. These values are based on the scale from the solitary solution (29). Indeed, further increase of the cut-off scales has little effect on the solutions (although numerical difficulties could occur when the cut-off scales are a factor two larger; in that case a converged solution becomes difficult to obtain). The heavy curve shows the minimum value of η of the axisymmetric solution at $r = 0$ versus ϵ and the thinner curve shows the minimum η of the rectilinear solution at $X = 0$. Since the horizontal scale for the solution ($\sim \epsilon^{-1/2}$) becomes very large as $\epsilon \to 0$, the axisymmetric and rectilinear

solutions start at $\epsilon = -0.01$ and -0.02, respectively. For $\epsilon < 0$, the dashed portions of the subcritical curves are unstable, which can be shown via the time-dependent solutions of the initial-value problem. These portions would be straight lines without the cubic-order term. No upper-branch solution is found on the supercritical side corresponding to $\epsilon > 0$. For the axisymmetric solution, the upper subcritical branch encounters a turning point at $\epsilon \approx -0.072$, and continues onto a forward stable branch of solution indicated by the solid line. The stable branch has significantly larger deformation amplitude and the solution of this branch eventually becomes supercritical. Likewise, the turning point for the rectilinear solution occurs at a slightly lower $\epsilon \approx -0.02$. In general, for a given ϵ value, the rectilinear deformation appears shallower than the corresponding axisymmetric deformation.

When F becomes larger, the magnitude of $\eta(0)$ at the turning point of the branches also becomes larger. In the inset of figure 3(*a*), we show the branches of solutions corresponding to $F = 0.33$ above $\eta = -1$. Since this value corresponds to the lower wall, rupture of the interface will take place before $\eta = -1$, leading to the formation of a dry spot. The result in the inset suggests that the lower-branch solutions cannot exist much further away from the turning point because of rupture. Since the amplitude of deformation increases rapidly with ϵ, the stable steady-state solution prior to rupture occurs only for a narrow range of ϵ.

As for the shapes and amplitude, the upper and lower branches of solutions are quite distinct other than near the turning point. To compare the shapes of the two solutions, we provide two three-dimensional plots of the equilibrium axisymmetric solution $\eta(r)$ at $\epsilon = -0.02$ for the case of $F = 0$. The unstable solution has the shape of a cone and the stable solution has the shape of a bowl; the two plots are shown in figures 3(*b*) and 3(*c*), respectively. The bowl-shaped solution has a significantly larger amplitude and flatter bottom. It is of interest to provide a comparison between the axisymmetric solution and the rectilinear solution. Again consider the case of $F = 0$ and at $\epsilon = -0.02$ as shown in figure 3(*d*); the heavy lines represent the axisymmetric solution and the thin lines represent the rectilinear solution.

We have also computed but do not show here the axisymmetric branch of solution for $F = 0$ and $B_v = 30$, which is significantly larger (note that in the experiments of VanHook *et al.*, the authors used $B_v = 18$, according to their table 2). The branch resembles the one shown in figure 3(*a*). Indeed, the shift between the two branches at $B_v = 1$ and 30 is small. For example, at $B_v = 1$ the turning point occurs at $\epsilon \approx 0.072$, with $\eta(0) \approx -0.52$. At $B_v = 30$, these values are $\epsilon \approx 0.077$, and $\eta(0) \approx -0.46$, respectively. However, the horizontal scale of the localized deformation becomes significantly smaller at $B_v = 30$ than at $B_v = 1$. The numerical solutions at $B_v = 30$ can be obtained with a cut-off value $r_{co} = 8$ instead of 20. Later, in regard to figure 7(*b*), we shall discuss a stable forward branch solution obtained via time simulation. In that case, comparison between our analysis and experiment will be discussed in greater detail.

For $F > 0.5$, the equilibrium solitary solutions become elevated. By including the cubic term, the instability becomes even stronger at larger values of F than without the term. In this case, there will be no forward branch of solution. However, it should be remembered that motion of the fluid in the upper layer has been ignored in the model.

4. Control strategy and analysis

A number of authors have demonstrated that a linear feedback control can delay the critical point to higher values for certain fluid states (see Tang & Bau 1994, 1998; Shortis & Hall 1996; and Joshi, Speyer & Kim 1997). Because of the possibility of

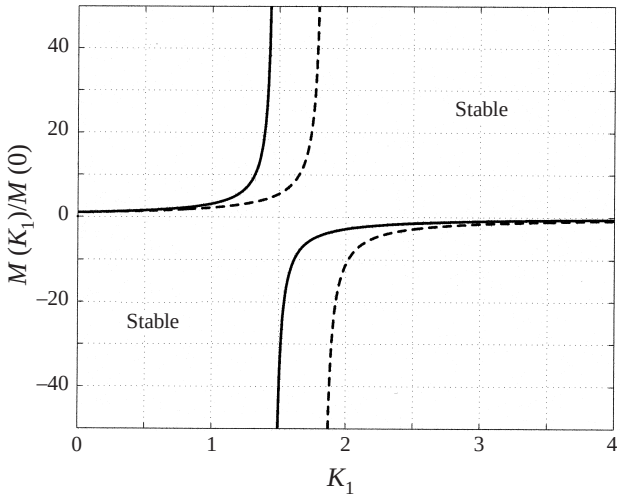

FIGURE 4. Delay of onset of long-wavelength convection as a function $\hat{K}_1$ for the cases of $F = 0.33$ (solid line) and $F = 0.66$ (dashed line). The second pair of curves to the right is included to show the destabilizing effect of the gain on a stable case when the layer is heated from above (where $M < 0$).

subcriticality, however, the region below the new critical point in the presence of control need not be completely stable. Disturbances can still grow exponentially to large amplitude if subcritical finite-amplitude steady solutions exist but are unstable. In order to guarantee that the no-motion state for our problem is stable even for such disturbances, our control strategy is nonlinear with the primary aim of eliminating the possibility of a subcritical solution by eliminating the quadratic nonlinear effect. We restrict the higher-order analysis to the proximity of the shifted critical point so that only the re-scaled version of (21) will be examined.

Increasing M_c

In deriving (21), the scaling relationship $\epsilon - \hat{K}_1 = q^2 R$ has been used. The critical control parameter corresponding to $R = 0$, with K_1 substituted for $\hat{K}_1$, gives

$$\epsilon - \hat{K}_1 = \frac{3D}{2(1+H)}\left((1+F)(1+H) - K_1\right) - 1 = 0. \tag{38}$$

In the fluid we consider, M is positive for heating from below, and so we require $D > 0$. When (38) is cast in terms of M_c, it gives

$$M_c(K_1) = \frac{2}{3}\frac{G(1+H)}{(1+H)(1+F) - K_1}. \tag{39}$$

The ratio $|M_c(K_1)/M_c(0)|$ measures the degree of stabilization. When this ratio is greater than one, the control exerts a stabilizing effect. Below one, the control is destabilizing. The ratio of the Marangoni numbers is given by

$$\frac{M(K_1)}{M(0)} = \frac{1}{1 - K_{1,eff}}, \tag{40}$$

where $K_{1,eff} = K_1/(1+F)(1+H)$. A typical linear stability diagram is shown in figure 4. In the results, we let $H = 0.1$, which is appropriate for a gas–liquid layer. The pair of solid curves corresponds to the case $F = 1/3$, and the pair of dashed curves

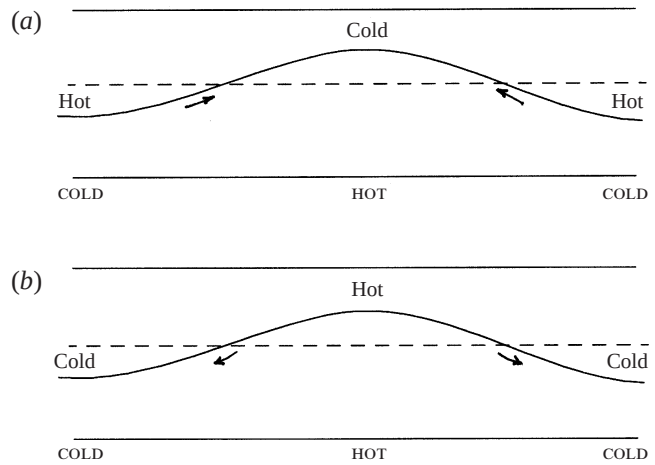

FIGURE 5. Sketch showing how a bottom modulated temperature can stabilize or destabilize the fluid at the interface. (*a*) Bottom heating is designed to reduce the vertical temperature gradient at the interface. Cold spots pull fluids from the hotter surrounding. The layer may still be unstable if the basic gradient is sufficiently strong. (*b*) When the bottom heating is strong enough, the high and low spots become hot and cold, respectively. When this happens, the high spots will be pulled apart by the surrounding low spots. The layer is unconditionally stable in this case.

corresponds to $F = 2/3$. The top-left and bottom-right regions outside the curves are unstable. As the gain K_1 increases from zero, the critical value of M increases from $M(0)$ to positive infinity at $K_{1,eff} = 1$. For $K_1 > (1 + H)(1 + F)$ the layer will always be stable on the basis of a linear theory if the fluid has $M > 0$. Complete stabilization is therefore easiest to achieve for low values of H and F. In contrast to the result of Bau (1999) for the onset of stationary convection, we conclude that $\partial M/\partial K_1 > 0$ as $q \to 0$ for the case considered here ($F > 0$, or $k > k_g$).

The physical mechanism for the stabilizing effect is now explained for the case of $M > 0$ with the aid of figure 5. At $K_1 = 0$, an elevated (depressed) region is cooler (warmer) than the undeflected interface. A cooler spot pulls fluid from surrounding warmer regions to feed the growing elevated region. As K_1 increases, the elevated (depressed) region becomes warmer (cooler), and so stabilization occurs. The argument to this point is similar to that of Tang & Bau (1994) for Rayleigh–Bénard convection. At $K_1 = (1 + F)(1 + H)$, the tangential gradient of temperature on the interface vanishes. For $K_1 > K_1^*$, the elevated (depressed) region becomes a warm (cold) region and is pulled downwards by surrounding cold fluid. This explains why (40) gives another branch of the critical curve which emerges from negative infinity. This curve is relevant when the surface tension of the fluid increases with temperature, i.e. when M is negative. Below this branch, the region is unstable. As K_1 increases away from K_1^*, this lower branch tends to zero indicating complete destabilization (which also occurs as $K_1 \to -\infty$ for $M > 0$). A large gain is required for building up the reversed interfacial thermal gradient needed to drive the long-wavelength convection for a layer of fluid with $M < 0$. We note in passing that a general analysis of the case $M < 0$ needs to include the possibility of oscillatory disturbances. For larger wavenumbers and values of K_1 roughly an order of magnitude greater than we consider, Bau (1999) has shown that oscillatory instability cannot only occur for $M > 0$ but can be more unstable than the monotonic instability. This kind of oscillatory instability seems to be associated with large values of gain and occurs also

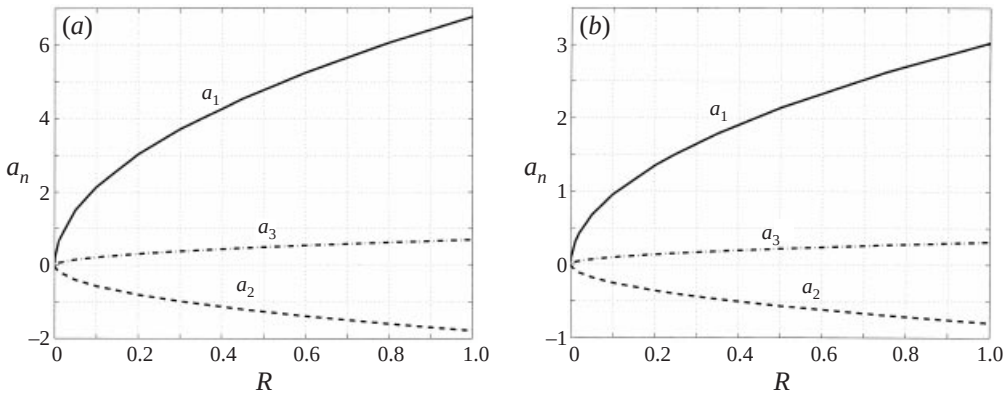

FIGURE 6. Curves showing three half-branches of the symmetric pitch-fork bifurcation corresponding to the first three leading Fourier coefficients for $\alpha = 0$ and (*a*) $\beta = -0.1$ and (*b*) $\beta = -0.5$.

for Rayleigh–Bénard convection; see Tang & Bau (1994). For $\hat{K}_i \sim O(1)$, (15) and (21) do not allow oscillatory solutions as $q \to 0$.

Nonlinear control and supercritical solutions

Apart from the coefficients, (21) has the same form as (32) discussed above. Unlike (32), in which the two coefficients of the nonlinear terms are determined from the imposed parameter values, the values of the two control coefficients α and β can be adjusted in (21) to achieve the desired effect. We will again concentrate on one-dimensional disturbances. Although it is important to consider more general disturbances, the basic ideas of this paper can be conveyed by means of a one-dimensional analysis.

First, we consider the case $\alpha = 0$. This case corresponds to a perfect cancellation of the quadratic nonlinear term. We shall obtain the bifurcation curves by the Fourier method. Since the equation contains only even-order spatial derivatives, A can be considered either of even or odd parity, such as

$$A = \sum_{n=0}^{Nt} a_n \cos nkX, \tag{41}$$

where Nt is a cut-off integer and k is the wavenumber. Periodic lateral boundary conditions are assumed based on the above solution form. The constant term a_0 corresponds to a shift in reference level, which has to be determined from mass conservation. All coefficients except for a_0 are determined from the evolution equation based on the above expansion. The linear neutral curve is again given by $R = k^2/B$ with the critical wavenumber occurring at $k = 0$, which allows us to scale the wavenumber according to $k = k_1(BR)^{1/2}$, so that k_1 varies between zero and 1. The Fourier coefficients can be arranged in a vector form and the equation becomes a set of first-order coupled ordinary differential equations, denoted by a vector equation $\dot{\boldsymbol{x}} = \boldsymbol{f}(\boldsymbol{x})$. In the following example, we let $k_1 = 0.18$. The equilibrium solution is again obtained by using the Newton–Raphson method. In the solutions we observe that all coefficients a_n with even index n ($n \geqslant 2$) vanish. Well-converged solutions are achievable with $Nt = 8$. In figures 6(*a*) and 6(*b*) we show the three leading coefficients, a_1 (solid), a_3 (dashed) and a_5 (dashed-dotted) as functions of R for two β values: -0.1 and -0.5, respectively. It is noted that, with negative β, the solution will be different from the modified solitary-type solutions of (30). The bifurcation

is of the pitch-fork type and in the figures only one of the two pitch-fork branches is shown. The other branch (not shown) is a mirror reflection about the horizontal axis. The relative magnitudes of the coefficients shown also indicate a fairly rapid convergence with respect to Nt. Comparing the same curves between figures 6(a) and 6(b), we see that for a given R the magnitudes of the coefficients for $\beta = -0.5$ are considerably smaller than those for $\beta = -0.1$. A larger $|\beta|$ is associated with a stronger stabilizing influence. The stability of the steady solution can be determined by integrating the equation $\dot{\boldsymbol{x}} = \boldsymbol{f}(\boldsymbol{x})$ using an initial condition perturbed slightly from the steady solution. The steady solution is found to be stable. So far, no other steady solution with the same wavenumber based on the form (41) has been found. In the uncontrolled problem discussed in § 3.2 the finite difference method was used for the localized disturbances. Here, the Fourier method is used to obtain periodic solutions. But it has been established that both methods indeed give the same numerical results.

It is now desirable to provide a summary of the previous results concerning how to compute the control gains. Assume that the values of F and H are given. Our goal in using control is to achieve a certain forward shift in D_c (therefore M_c and ϵ) and also a value of β for the coefficient of the cubic term corresonding to a supercritical bifurcation. Based on these inputs we compute D_c and K_i ($i = 1, 2, 3$) from the following equations:

$$D_c = \frac{2(1+\epsilon)}{3(1+F)}, \tag{42a}$$

$$\hat{K}_1 = \epsilon\ , \quad K_1 = \frac{2(1+H)\hat{K}_1}{3D_c}, \tag{42b}$$

$$\hat{K}_2 = F - \tfrac{1}{2} - \tfrac{1}{2}a_2\hat{K}_1, \quad K_2 = \frac{2(1+H)\hat{K}_2}{3D_c}, \tag{42c}$$

$$\hat{K}_3 = \tfrac{1}{3}(\beta_0 + \beta_1\hat{K}_1 - \beta), \quad K_3 = \frac{2(1+H)\hat{K}_3}{3D_c}, \tag{42d}$$

where $a_1 = 2(1 - H(1+F))$ and β_0 and β_1 are given by (22a, b), respectively. Note that the D_c as well as the control gains do not depend on B. The result for a selected group of inputs is summarized in table 1, in which the results are based on $H = 0.1$. The result indicates that in general larger values of K_1 and K_3 are required to control the instability for larger values of F. It is also advantageous to have $a_1 > 0$ if $\hat{K}_1 > 0$ (i.e. $\epsilon > 0$) in order to reduce the size of $\hat{K}_2$, i.e. have $H(1+F) < 1$. In another study employing nonlinear feedback control strategy by Shortis & Hall (1996), it is remarked that the delay of convection by means of a linear feedback can give rise to subcritical instability. Here, we found that a quadratic term of $O(a_1\hat{K}_1)$ is responsible for generating subcritical instability.

5. Direct time simulations

Equations (18), (21) and (32) can be solved as initial-value problems by means of a finite-difference approach. The time-dependent solutions allow us to examine stability from a different point of view. In the integration of the one-dimensional form of the equation, we assume a periodic boundary condition at the two end points and impose a mass conservation condition which serves to modify the free-surface level in the presence of deformation. Below we provide a few representative examples. The initial

F	ϵ	β	D_c	K_1	K_2	K_3
0.33	0.50	0.00	0.75	0.49	−0.59	0.54
0.67	0.50	0.00	0.60	0.61	−0.30	1.18
0.33	0.50	−0.50	0.75	0.49	−0.59	0.70
0.67	0.50	−0.50	0.60	0.61	−0.30	1.38
0.33	1.00	−0.50	1.00	0.73	−0.76	0.86
0.67	1.00	−0.50	0.80	0.92	−0.61	1.49

TABLE 1. Values of control gains computed from selected parameters.

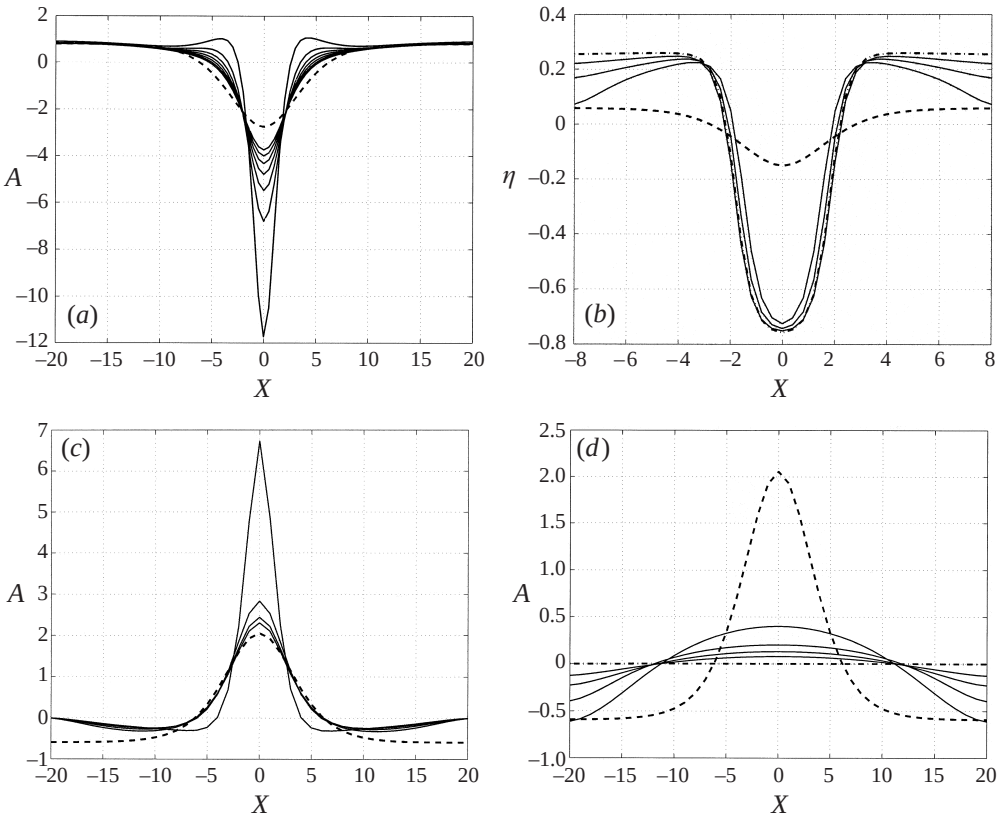

FIGURE 7. Direct time simulaton showing (*a*) divergence in time of a sufficiently large-amplitude disturbance near a steady, subcritical solution branch; (*b*) convergence to a finite-amplitude stable equilibrium with parameters under experimental conditions when the stabilizing cubic nonlinear term is included in the equation; (*c*) the divergent behaviour of an elevated localized disturbance at $B = 1$, $F = 0.67$ and $R = -0.2$ and with no control; (*d*) the decay of the same disturbance as in (*c*) when control is imposed with parameter values $\alpha = -0.5$ and $\beta = -0.1$. See the text for details.

disturbance shape corresponds to a steady-state solitary deformation because this is the most 'dangerous' disturbance for $K_i = 0$.

Consider an example for (18) with $F = 0.33$ and $B = 1$. First, we show that if the amplitude of a localized disturbance is sufficiently large, then it will diverge even when the value of R is subcritial. Let us assume that $R = -0.2$. Figure 7(*a*) shows an initial disturbance corresponding to a depressed solitary deformation of

amplitude $2|A_s|$ (dashed curve), where A_s is the equilibrium value from (29). For mass conservation we impose the constraint $\int A \mathrm{d}X = 0$. In the integration, a time step of 2×10^{-3} is used. The solid curves show the divergence in time, with the first curve corresponding to 5000 time steps. In the plot, consecutive curves are separated by 1000 steps. The divergence becomes very rapid after 10^4 time steps. On the other hand, if the initial localized disturbance has amplitude less than that of the dashed curve, the disturbance will eventually damp out and the static no-motion state will resume. For $R > 0$, however, disturbances will diverge even for small amplitudes. For small values of F, the rate of divergence is less severe for the same disturbance amplitude.

As a comparison to the diverged solution, we consider a second example for a stable depressed solution. In figure 7(*b*), we consider a smaller $F = -0.07$, $B_v = 18$ and ϵ to be slightly supercritical at 0.05. The value of F is the same as that for figure 21 of the experiments (VanHook *et al.* 1997). The value of ϵ is supercritical, roughly corresponding to the mean condition of the experiment. Here, B_v is equal to their static Bond number, which is equal to 18 according to the value of their table 2. The time simulation here is based on the one-dimensional rectilinear version of (32) with strong surface tension, so that the effect of the cubic nonlinear term is included. In this example, there exists a stable finite-amplitude solution corresponding to a forward branch. The initial disturbance prescribed is a solitary-shaped localized disturbance (dashed curve). The time step used for integration of this case is equal to 0.02. The three solid curves represent the solutions sampled at 5×10^3 steps. The dashed-dotted curve corresponds to the solution at the end of 1.2×10^5 steps. A reasonably well-converged steady-state solution is achieved as shown. Now we show that the horizontal scale from the simulated steady solution is indeed consistent with the scale of the mode observed in the experiments (see VanHook *et al.* 1997). According to the description of the experiment, the liquid layer sits on a gold-plated aluminium mirror of diameter-to-liquid-thickness ratio, L/d, $\sim 2.25 \times 10^2$ (based on a diameter of 3.81 cm and an averaged d value of 0.017 cm). Considering a period of the disturbance based on the maximal length scale of the mirror, we obtain $q \sim 0.03$. In our simulation, the horizontal extent of figure 7(*b*), measured in ΔX, is equal to 16. Now if we let $q\Delta X$ equal $L/d = 225$, we obtain $q = 0.07$, which is on the same order of magnitude as the experimental value.

Lastly, we demonstrate how the control stabilizes an otherwise unstable case for which the interface diverges. Consider again $B_v = 1$ but now $F = 0.67$. We choose $F > 0.5$ for this case because it represents a more unstable situation than the previous $F < 0.5$ case. If the control works for this situation, we argue that it will work even better for the more stable situation. Figure 7(*c*) shows again how an initially prescribed localized disturbance (at $1.5A_s$) diverges in time without control, based on (18). Again, the dashed line shows the initial disturbance shape. The subcritical condition corresponds to $R = -0.2$. The first solid line corresponds to 5000 steps after the start of integration with a time step of 0.01, and a sampling period of 2000 steps is used thereafter for the curves associated with increasing amplitude. In figure 7(*d*), with the same initial localized disturbance (dashed line), time step of integration, and values of R, F and B as in figure 7(*c*), we now study the time behaviour by imposing the values of control parameters at $\alpha = -0.5$ and $\beta = -0.1$, using (21). The four thin solid lines show the subsequent disturbance shape at 10^4 steps apart. The dashed-dotted line shows the disturbance shape at the end of 4×10^5 steps. The otherwise diverging disturbance converges to the no-motion state in a slow fashion when the control is invoked. In fact, a more rapid decay is possible by increasing the magnitude of β. The sign of α appears to be insignificant to the control.

6. Concluding remarks

In this paper we have analysed a strategy for controlling long-wavelength Marangoni–Bénard convection. Based on the re-scaled version of the evolution equation near the critical point, a family of steady-state subcritical solutions of cnoidal-type was found. In order to demonstrate the dynamical effect of the next-order nonlinearity, the strong-surface-tension assumption is invoked, and a stable forward branch is obtained for both the rectilinear and axisymmetric cases. Stable forward branches for other cnoidal-type solutions will certainly be present, although only disturbances of the localized type have been investigated here.

The strategy of control discussed in this paper basically is to alter values and signs of the linear and lower-order nonlinear coefficients. With control, subcritical solutions can be suppressed. The bifurcation properties of the supercritical solutions are investigated with and without detuning. The results demonstrate that the strategy is effective for controlling the long-wavelength instability. Lastly, a few examples are provided to show the unstable growth of a disturbance without control and how such unstable disturbances can be damped out by applying the control temperature at the wall.

We have focused mainly on disturbances of a localized type in the analysis. Other disturbances, such as those of cnoidal type, can certainly become unstable in the absence of control. But with control, we can basically eliminate the entire family of cnoidal modes by eliminating the quadratic nonlinear term from the evolution equation. The analysis needs to be generalized in order to demonstrate the control of three-dimensional instabilities, and eventually, the model must be made more realistic to reflect the obvious fact that sensing and control is unlikely to be done on a truly continuous basis. However, we believe that such refinements will not change the basic conclusions of this analysis.

This research is supported by grants from NASA Microgravity Fluid Physics Program (Grant no. NAG3-1819) and from the United States Air Force (Grant no. F49620-93-1-0332).

REFERENCES

Abramowitz, M. & Stegun, I. A. 1972 *Handbook of Mathematical Functions*, pp. 567–573. Dover.

Bau, H. H. 1999 Control of Marangoni–Bénard convection. *Intl J. Heat Mass Transfer* **42**, 1327–1341.

Deissler, R. J. & Oron, A. 1992 Stable localized patterns in thin liquid films. *Phys. Rev. Lett.* **68**, 2948–2951.

Funada, T. 1987 Nonlinear surface waves driven by the Marangoni instability in a heat transfer system. *J. Phys. Soc. Japan* **56**, 2031–2038.

Funada, T. & Kotani, M. 1986 A numerical study of nonlinear diffusion equation governing surface deformation in the Marangoni convection. *J. Phys. Soc. Japan* **55**, 3857–3862.

Joshi, S. S., Speyer, J. L. & Kim, J. 1997 A systems theory approach to the feedback stabilization of infinitesimal and finite-amplitude disturbances in plane Poiseuille flow. *J. Fluid Mech.* **332**, 157–184.

Oron, A., Davis, S. H. & Bankoff, S. G. 1997 Long-scale evolution of thin liquid films. *Rev. Mod. Phys.* **69**, 931–980.

Scriven, L. E. & Sternling, C. V. 1964 On cellular convection driven surface tension gradients: effects of mean surface tension and surface viscosity. *J. Fluid Mech.* **19**, 321–340.

Shortis, T. A. & Hall, P. 1996 On the effect of feedback control on Bénard convection in a Boussinesq fluid. *NASA Contractor Rep.* 198280; *ICASE Rep.* 96-9.

Simanovskii, I. B. & Nepomnyashchy, A. A. 1993 *Convective Instabilities in Systems with Interface*. Gordon and Breach.

Smith, K. A. 1966 On convective instability induced by surface tension. *J. Fluid Mech.* **24**, 401–414.

Tang, J. & Bau, H. H. 1994 Stabilization of the no-motion state in the Rayleigh–Bénard problem. *Proc. R. Soc. Lond.* A **447**, 587–607.

Tang, J. & Bau, H. H. 1998 Experiments on the stabilization of the no-motion state of a fluid layer heated from below and cooled from above. *J. Fluid Mech.* **363**, 153–171.

VanHook, S. J., Schatz, M. F., Swift, J. B., McCormick, W. D. & Swinney, H. L. 1997 Long-wavelength surface-tension-driven Bénard convection: experiment and theory. *J. Fluid Mech.* **345**, 45–78.

Yuen, P. K. & Bau, H. H. 1996 Rendering a subcritical Hopf bifurcation supercritical. *J. Fluid Mech.* **317**, 91–109.